Gim *et al. Nano Convergence* (2026) 13:8
https://doi.org/10.1186/s40580-026-00541-5

Nano Convergence

FULL PAPER Open Access

Correlating nanoscale electronic uniformity and device performance in mixed-cation perovskite solar cells driven by sequential deposition

Yeonseo Gim[1,2], Ha Kyung Park[1], Geumha Lim[1,2], Jihyun Kim[1], Yeon Soo Kim[3,4] and William Jo[1,2*]

Abstract
Perovskite solar cells have garnered substantial attention in recent years owing to their high efficiency and the tunable bandgaps of their perovskite absorbers. Among various fabrication techniques, vacuum-based thermal evaporation offers particularly advantageous by minimizing environmental influences such as humidity, thereby enabling enhanced phase stability and reproducibility. In particular, sequential thermal evaporation allows precise control over the deposition rate, thickness, and stacking order of individual precursor layers, providing a versatile platform for nanoscale materials engineering. In this study, mixed-cation perovskite thin films based on formamidinium lead iodide ($FAPbI_3$) and cesium lead iodide ($CsPbI_3$) were fabricated via sequential thermal evaporation. By optimizing the deposition sequence of organic and inorganic precursors, a well-defined solid-state diffusion pathway was established for efficient Cs^+ incorporation into the perovskite layer. Structural and optical analyses, including X-ray diffraction and photoluminescence spectroscopy, revealed that Cs^+ incorporation stabilizes the alpha-phase and enhances crystallinity while suppressing non-radiative recombination. Among the optical characterization, time-resolved photoluminescence and surface photovoltage measurements demonstrate prolonged carrier lifetimes, a stabilized local potential landscape under illumination, and reduced charge trapping. These structural and electronic enhancements resulted in superior device stability and performance, characterized by improved photocurrent generation and suppressed *J-V* hysteresis. As a result, the fill factor and the short-circuit current density increases and the power conversion efficiency of the devices improved dramatically—from 8.89% to 16.88%. Overall, this work demonstrates that sequential deposition engineering serves as a critical nanoscale design strategy for controlling cation distribution and phase stability in vacuum-processed perovskite thin films, thereby enabling robust and high-performance perovskite solar cells.

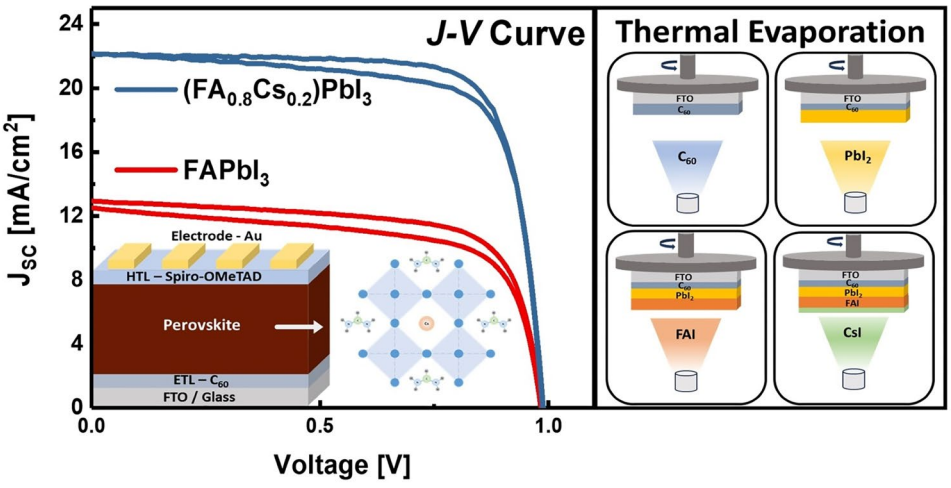
Keywords Perovskite solar cells, Vacuum deposition, Sequential deposition, Metal halide perovskite

*Correspondence:
William Jo
wmjo@ewha.ac.kr

Full list of author information is available at the end of the article

© The Author(s) 2026. **Open Access** This article is licensed under a Creative Commons Attribution-NonCommercial-NoDerivatives 4.0 International License, which permits any non-commercial use, sharing, distribution and reproduction in any medium or format, as long as you give appropriate credit to the original author(s) and the source, provide a link to the Creative Commons licence, and indicate if you modified the licensed material. You do not have permission under this licence to share adapted material derived from this article or parts of it. The images or other third party material in this article are included in the article's Creative Commons licence, unless indicated otherwise in a credit line to the material. If material is not included in the article's Creative Commons licence and your intended use is not permitted by statutory regulation or exceeds the permitted use, you will need to obtain permission directly from the copyright holder. To view a copy of this licence, visit http://creativecommons.org/licenses/by-nc-nd/4.0/.

Graphical abstract



1 Introduction

Perovskite solar cells (PSCs) have garnered widespread attention in recent years owing to their high efficiency and the tunable bandgaps of their perovskite absorber materials. In particular, the efficiency of organic–inorganic mixed lead halide PSCs has risen sharply over the past few decades, owing to their exceptional photovoltaic properties, including long carrier diffusion lengths and strong light absorption [1, 2]. Furthermore, the perovskite materials used in these solar cells feature bandgaps that are well-suited for solar energy capture, contributing to efficiency improvements. Consequently, the highest reported efficiency of these solar cells has now reached 26% [2–7].

Among the various solar cell manufacturing techniques explored to date, research on thermal evaporation (TE) has progressed rapidly, with reported efficiencies reaching 24% [8, 9]. The vacuum TE method, in particular, has garnered attention as an environmentally stable approach suitable for large-area deposition, making it a promising candidate for commercial applications [10]. Fabrication methods for perovskite can be categorized according to the deposition process [11]. Specifically, TE-based perovskite synthesis encompasses several approaches, including co-evaporation, sequential deposition, and single-source evaporation. Co-evaporation involves the simultaneous evaporation of multiple precursor materials. In contrast, single-source TE allows uses pre-synthesized materials, allowing precise control over thickness, partial pressure, and deposition rate during film deposition. Sequential TE inherits advantages of single-source TE to enable the stepwise deposition of multiple materials. As illustrated in Fig. 1, C_{60}, PbI_2, FAI, and CsI were sequentially deposited onto the substrate via TE.

Among the various metal halide perovskite materials synthesized so far, formamidinum lead iodide ($FAPbI_3$) has been identified as an optimal material for single-junction PSCs [12]. In particular, perovskites with mixed A-site cations in the ABX_3 structure have been demonstrated to enhance photovoltaic properties and thermal stability. Specifically, among known PSCs, those based on $FAPbI_3$ has shown the highest efficiency [13]. Both $FAPbI_3$ and cesium lead triiodide ($CsPbI_3$) possess ideal bandgaps for solar light absorption and exhibit superior thermal stability compared to methylammonium lead iodide [14, 15]. Notably, the inorganic $CsPbI_3$ material shows strong potential for solar cells owing to its excellent phase stability and resistance to degradation [16, 17]. Despite these advantages, both $FAPbI_3$ and $CsPbI_3$, which black α-phase exhibits photovoltaic properties, tend to transition to the yellow δ-phase at room temperature, so stabilizing the α-phase remains a key challenge in advancing device performance [18, 19]. To address this issue and enhance charge transport properties, researchers have explored cation and halide mixing and this approach has resulted in PSC efficiencies exceeding 18% [20].

The size of A-site cations plays a crucial role in determining the structural stability of perovskites. This stability is commonly assessed using the Goldschmidt tolerance factor (t), which is given as [21].

$$t = \frac{r_A + r_x}{\sqrt{2}(r_B + r_x)}, \tag{1}$$

where r_A, r_B, and r_X denote the effective radii of the A, B, and X ions, respectively. In general, a t value between 0.8 and 1 results in a stable cubic perovskite structure, while values outside this range result in non-perovskite phases

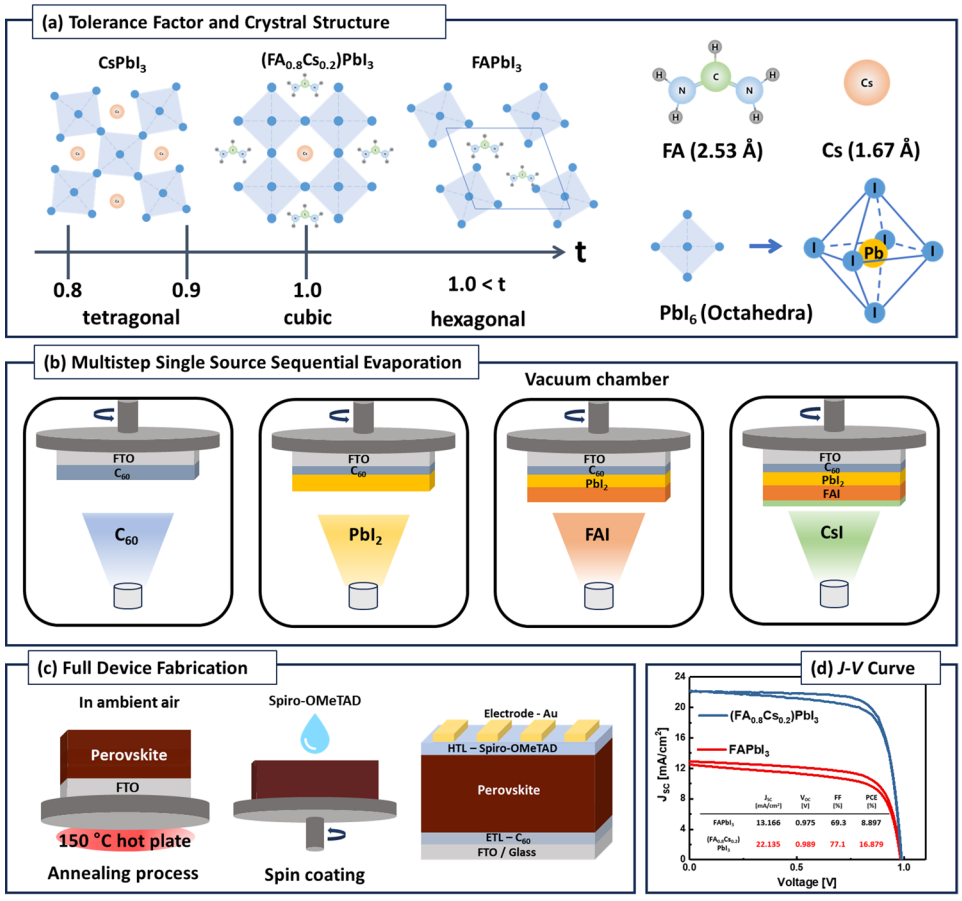


Fig. 1 **a** Tolerance factors (t) and crystal structure of halide perovskite. Cation diagram of the FA molecule, Cs, and PbI_6 (Octahedra). **b** Schematic illustration of multistep single-source sequential evaporation for thermally evaporated PSCs. PbI_2, FAI, and CsI sources were sequentially deposited layer by layer. **c** After the annealing process, the hole transport layer was deposited by spin coating, followed by TE of a gold electrode to fabricate the full device. **d** Current density–voltage (J–V) curve of the fabricated device

Table 1 Effective cation radius and effective tolerance factor as a function of FA and Cs composition. For mixed compositions, we use $(FA_XCs_{1-X})PbI_3$. The unit of r_{eff_cation} is [Å]

X	1-X	r_{eff}	t_{eff}
1	0	2.530	1.0387
0.9	0.1	2.444	1.0198
0.8	0.2	2.358	1.0009
0.7	0.3	2.314	0.9913

[22, 23]. Among A-site cations, FA^+ exhibits a high tolerance factor owing to its relatively large ionic radius (2.53 Å), whereas Cs^+ features a smaller ionic radius. (1.67 Å) [24]. Consequently, incorporating both FA^+ and Cs^+ can improve structural stability [25]. When FA and Cs are mixed at the A site, their effective cation radius in $(FA_xCs_{1-x})PbI_3$ can be determined using the following equation [26]:

$$r_{eff_cation} = Xr_{FA} + (1 - X)\, r_{Cs}\,, \qquad (2)$$

Notably, substituting r_{eff_cation} into Eq. (1) yields the effective tolerance factor (t_{eff})..

As illustrated in Fig. 1, FA^+ is a molecular ion, whereas Cs^+ is a monoatomic cation. Given its larger ionic radius, FA^+ induces lattice strain when positioned at the A site of a perovskite crystal structure, increasing the tolerance factor [27]. Introducing Cs^+, which has a smaller radius, mitigates this strain and enhances the stability of the cubic structure. Table 1 summarizes the calculated t_{eff} values using Eq. (2), indicating that the optimal x value is 0.8.

To synthesize a stable mixed-cation perovskite thin film, this study adopted a single-source evaporation method. The process involved depositing an $FAPbI_3$ layer, followed by an additional CsI precursor layer. Separating the deposition of organic and inorganic materials allowed for independent process optimization: the deposition of FAI was vacuum pressure-controlled, whereas CsI required a constant deposition rate. This sequential evaporation allowed Cs^+ to diffuse effectively into the $FAPbI_3$ perovskite bulk layer during thermal annealing.

Consequently, the incorporation of Cs^+ led to the formation of highly stable crystal structures and a substantial enhancement in short-circuit current density (J_{SC}).

2 Experimental details

2.1 Device fabrication

The fluorine-doped tin oxide (FTO) coated glass was cleaned by sonication in deionized water, isopropyl alcohol and acetone for 15 min, respectively. 15 nm of C_{60} (> 99.99%, Sigma Aldrich) layer was deposited using TE method and the deposition rate was 0.1 Å/s. Perovskite precursor layer was deposited via sequential evaporating lead iodide (PbI_2, TCI Co.) and formamidinium iodide (FAI, Greatcell Solar) powder sources. Deposition rate for PbI_2 was 5 Å/s and nominal thickness was 1400 nm. Deposition rate of FAI organic salt was decided by vacuum level which was $2.0^{\sim}10^{-4}$ Torr for 10 min and at 5×10^{-5} Torr, deposition time was different as sample condition. Deposition rate for cesium iodide (CsI, Sigma Aldrich) inorganic salt was 1 Å/s and the nominal thickness was different as condition of ratio. In all TE processes, the deposition rates and nominal thicknesses of each material were precisely monitored and controlled using a quartz crystal microbalance (QCM) sensor (Figure S1). The deposition parameters were precisely controlled to maintain a uniform final thickness of 670 nm across all perovskite samples. Chamber was evacuated after the deposition of every layer. Perovskite precursor layer was annealed in the ambient atmosphere at 150 ℃ for 90 s using a hot plate to form perovskite phases. Thickness of annealed perovskite thin film was 670 nm. The 2,2',7,7'-Tetrakis[N, N-di(4-methoxyphenyl) amino]-9,9'-spirobifluorene (Spiro-OMeTAD) solution was prepared with 72.3 mg of Spiro-OMeTAD powder with 35 µL lithium bis (trifluoromethanesulfonyl) imide (LiTFSI) solution (260 mg in 1 mL of Acetronitrile) and 30 µL 4-*tert*-butylpyridine (tBP) in 1 mL of chlorobenzene. Hydrophilic filtered spiro-OMeTAD solution was spin-coated for 30 s with 2000 rpm. To complete the solar cell, 80 nm of Au top electrode was deposited by TE method.

3 Thin film and device characterization

Scanning electron microscopy (SEM) images was obtained using HITACHI SU8220 (Western Seoul Center KBSI) with acceleration voltage of 15 kV. X-ray diffraction pattern was obtained using (Expert pro-MPD, PANalytical) equipped with Cu Kα radiation (0.15418 nm), tension: 40 kV, current: 40 mA. Fourier transform-infrared spectrometer (Nicolet iS50, Thermo Fisher Scientific) was used to obtained spectrum. Secondary ion mass spectroscopy (SIMS) profile was performed at the National Center for Inter-university Research Facilities (NCIRF) at Seoul National University and obtained using TOF.SIMS-5 by Ar^+ etching. Especially, positive mode was used to detect the FA and Cs ions. Absorbance spectrum was obtained by UV-visible spectroscopy (Lambda 750, Perkin Elmer). FuoTime 300 (PicoQuant) was used to obtain photoluminescence (PL) spectrum with using a laser with wavelength of 405 nm and intensity of 4.5 mW. The time-resolved photoluminescence (TRPL) measured at the position of the PL peak in each sample. Kelvin probe force microscopy (KPFM) was performed using an atomic force microscope (MFP-3D Infinity, Oxford Instruments) equipped with a Ti/Ir - coated non-contact tip (Oxford Instruments) to obtain the contact potential difference (V_{CPD}) between the tip and sample, assuring the surface potential distribution. Surface photovoltage (SPV) measurements were performed using KPFM by monitoring the change in the V_{CPD} between dark and illuminated conditions. *J-V* characteristics was measured through (Keithley 4200) under 1 sun (100 $mWcm^{-2}$) condition (Sol3A Class AAA). During J-V measurements, a device was shielded by a black metal mask with an aperture area of 0.049 cm^2. J-V curves were measured from − 0.1 to 1.2 V for the forward scan and from 1.2 to -0.1 V for the reverse scan. External quantum efficiency (EQE) measurement was conducted using McScience K3100 IQX. EQE spectra were measured from 300 nm to 900 nm with a step wavelength of 10 nm.

The PSCs were structured as glass/FTO/C_{60}/perovskite/spiro-MeOTAD/Au. Figure 2 statistically compares the photovoltaic parameters and Table 2 presents the corresponding values for average of 36 samples and the best-performing PSCs. $(FA_{0.8}Cs_{0.2})PbI_3$ PSCs showed increased value in all parameters. Dots next to the boxes in the graph indicates that the distribution of values for $(FA_{0.8}Cs_{0.2})PbI_3$ PSCs is the narrowest, suggesting improved device-to-device reproducibility and enhanced nanoscale uniformity of the perovskite films.

The $(FA_{0.8}Cs_{0.2})PbI_3$ PSCs, which possess a Goldschmidt tolerance factor closer to one, exhibit the Favorable crystallinity, leading to pronounced improvements in charge transport-related parameters such as J_{SC} and FF. In detail, the average J_{SC} increased from 11.754 mA/cm^2 to 20.705 mA/cm^2, while FF also increased from 63.9% to 74.1%. These improvements suggest more efficient carrier collection and reduced recombination losses within the perovskite absorber. Also, V_{OC} values for $FAPbI_3$ and $FACsPbI_3$ were increased as Cs added and band gap was increased. These enhanced values led to an improvement in PCE. The best PCE of $(FA_{0.8}Cs_{0.2})PbI_3$ improved from 16.879% for $FAPbI_3$ to 8.897%, with a V_{OC} of 0.989 V, J_{SC} of 22.135 mA/cm^2, and FF of 77.1%. As the Cs content increases, which results in large band gap (E_g), the V_{OC} increases. These observations imply that the superior device characteristics of $(FA_{0.8}Cs_{0.2})PbI_3$ are closely related to changes in thin-film microstructure and defect

Results and Discussion

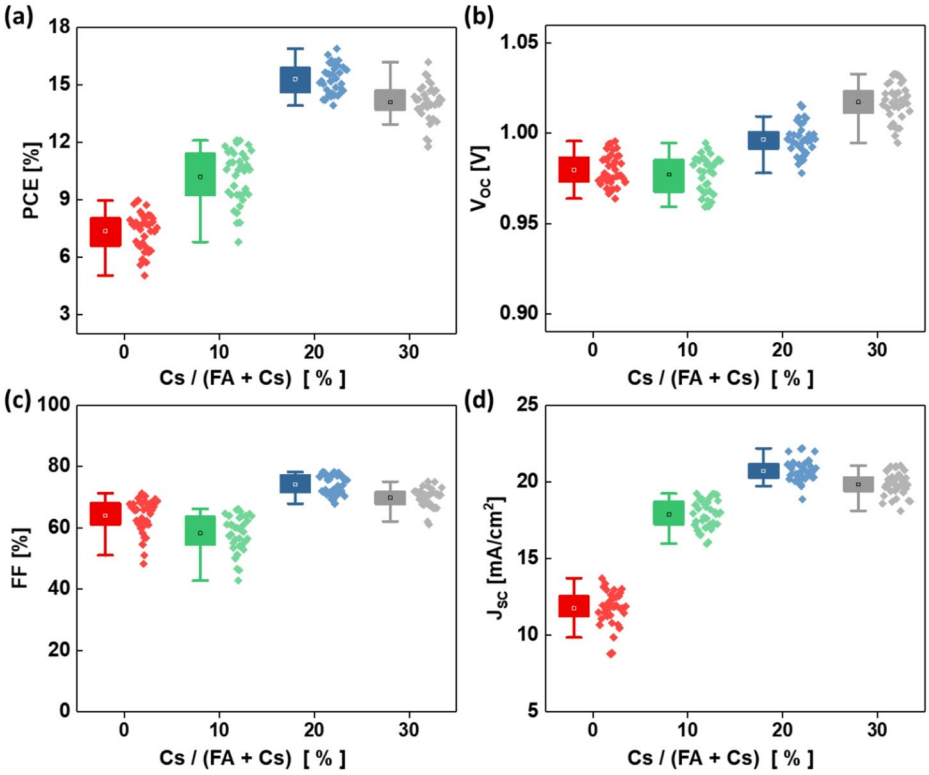


Fig. 2 Distribution of **a** PCE, **b** V_{OC}, **c** FF, and **d** J_{SC} for mixed-cation PSCs across 36 samples under four different conditions

Table 2 Average photovoltaic parameters (J_{SC}, V_{OC}, FF, PCE) of PSCs across 36 samples and corresponding values for the best-performing PSC

	J_{SC} [mA/cm^2]	V_{OC} [V]	FF [%]	PCE [%]
$FAPbI_3$	11.754 (13.166)	0.979 (0.975)	0.639 (0.693)	7.367 (8.897)
$(FA_{0.9}Cs_{0.1})PbI_3$	17.871 (19.213)	0.977 (0.986)	0.582 (0.639)	10.196 (12.088)
$(FA_{0.8}Cs_{0.2})PbI_3$	20.705 (22.135)	0.997 (0.989)	0.741 (0.771)	15.292 (16.879)
$(FA_{0.7}Cs_{0.3})PbI_3$	19.609 (20.998)	1.017 (1.028)	0.698 (0.749)	14.081 (16.172)

landscape induced by Cs incorporation during sequential evaporation. To understand the nanoscale factors governing device uniformity and charge transport, $FAPbI_3$ and optimized $(FA_{0.8}Cs_{0.2})PbI_3$ thin films were systematically compared in terms of cation diffusion, recombination behavior, and interfacial potential.

The phase transition from yellow to black indicated the conversion of $FAPbI_3$ from the non-photovoltaic δ-phase to the photovoltaic α-phase [28]. This macroscopic color change reflects the stabilization of the photoactive perovskite lattice, which is a prerequisite for nanoscale electronic uniformity. XRD analysis confirmed the crystallization and preferential orientation of the thin films. Figure 3(a) presents the XRD patterns with 2θ ranging from 10° to 30°. All samples displayed the strongest diffraction peak at approximately 14°, corresponding to the (100) crystal plane of the pure photovoltaic α-phase $FAPbI_3$ [29, 30]. This preferred orientation is known to facilitate vertical charge transport across the perovskite layer by minimizing structural discontinuities at the nanoscale. A peak at 19.8° was attributed to the (110) orientation of the α-phase $FAPbI_3$, while the peak at 28.2° corresponded to the (200) plane of α-$FAPbI_3$. Notably, for the $(FA_{0.8}Cs_{0.2})PbI_3$ perovskite thin film, the distinctive peak of the non-photovoltaic δ-phase (around 11.8°) was completely absent, and the primary (100) peak exhibited a higher intensity and a narrower full width at half maximum (FWHM), decreasing from 0.267° to 0.209°. According to the Scherrer equation, this reduction in FWHM indicates an increase in the crystallite grain size, which can effectively reduce grain boundary (GB) density and suppress defect-assisted carrier scattering at the nanoscale, thereby improving carrier mobility [31]. Fig. 3(b) presents a magnified view of the XRD peaks in the 2θ range of 12° to 15°. As the amount of Cs increased, the peak associated with excess PbI_2 at 13.1°

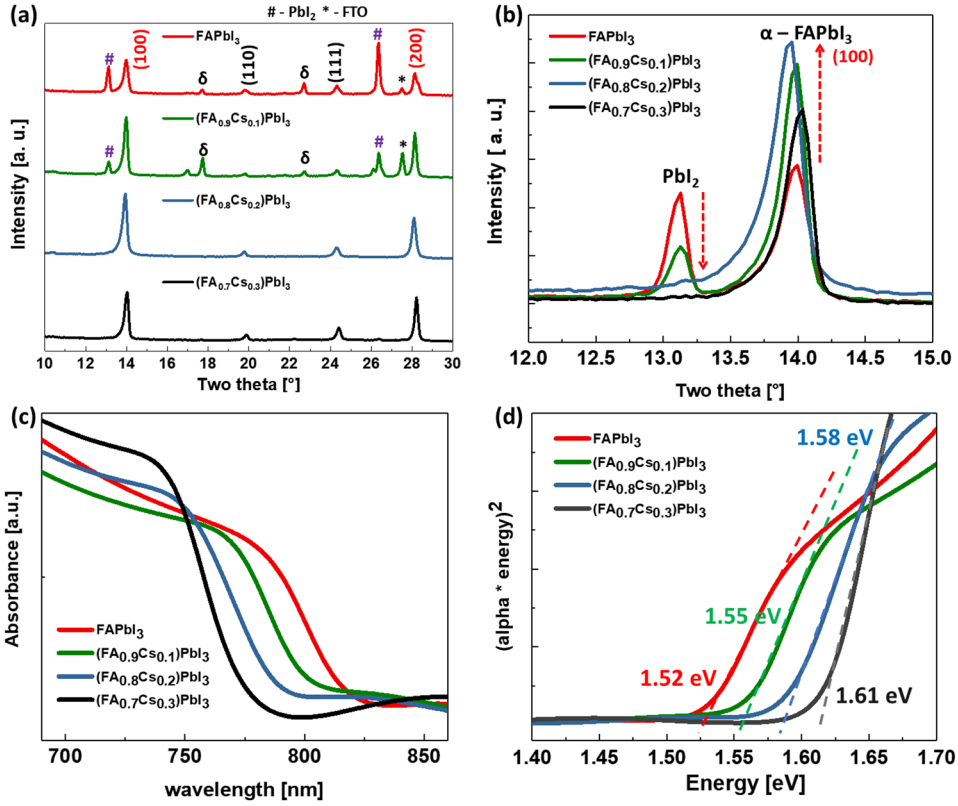


Fig. 3 **a** XRD patterns of perovskite films with various Cs contents. **b** Enlarged XRD peaks corresponding to the alpha phase (100) orientation of $FAPbI_3$. **c** UV-visible absorbance spectra of the perovskite films. **d** Tauc plots derived from the absorbance spectra for E_g determination

diminished, while that related to α-$FAPbI_3$ at 14.1° intensified, suggesting the complete conversion of PbI_2 into the photovoltaic α-$FAPbI_3$. The intensity of the (100) peak followed the order of $(FA_{0.8}Cs_{0.2})PbI_3$ > $(FA_{0.9}Cs_{0.1})PbI_3$ > $(FA_{0.7}Cs_{0.3})PbI_3$ > $FAPbI_3$. The slight shift of the peak from 14.1° to 13.9° with an increase in peak intensity indicates lattice relaxation and improved crystallinity, rather than a transition to δ-phase. This trend confirms that $(FA_{0.8}Cs_{0.2})PbI_3$ exhibits the highest crystallinity and forms a more stable lattice structure. However, excessive Cs^+ incorporation can disrupt the perovskite cubic phase.

The absorbance spectrum obtained from UV−Vis spectroscopy measurements was used to calculate the bandgap (E_g). Specifically, the E_g was determined using a Tauc plot, which represents the function $(\alpha h\nu)^2$, where α is the absorption coefficient, h is Planck's constant, and v is the photon frequency. Previous studies have reported that the Eg value of black-phase $FAPbI_3$ is 1.48 eV ~ 1.52 eV, while that of black-phase $CsPbI_3$ is 1.73 eV [15, 32]. In this study, the estimated E_g of black-phase $FAPbI_3$ was 1.52 eV, while E_g of $(FA_{0.8}Cs_{0.2})PbI_3$ was blue-shifted to 1.58 eV (Fig. 3(c, d)). This gradual blue shift reflects the formation of a mixed-cation alloy and a systematic modulation of the electronic band structure. As illustrated in Fig. 3(d), E_g increased slightly from 1.52 to 1.61 eV as the Cs ratio increased from 0% to 30%. Specifically, for every 0.1 decrease in *x*, the amount of CsI increased, resulting in an E_g shift of approximately 0.3 eV. These relatively small E_g variations are insufficient to explain the pronounced enhancements in device performance observed in Fig. 2. This indicates that the performance improvement does not primarily originate from bulk optical band gap tuning. Instead, nanoscale electronic properties such as defect-mediated recombination pathways and local potential distribution play a dominant role in governing charge transport and collection. Accordingly, the following sections focus on a detailed nanoscale investigation of carrier recombination dynamics and interfacial potential.

To clarify the impact of Cs incorporation, we selected $FAPbI_3$ and optimized $(FA_{0.8}Cs_{0.2})PbI_3$ as representative samples for a comparative nanoscale analysis, enabling a direct correlation between cation composition and electronic properties. KPFM topography images (Fig. 4(a, b)) revealed distinct morphological differences under different fabrication conditions. The $(FA_{0.8}Cs_{0.2})PbI_3$ perovskite films exhibited larger grain sizes compared to the $FAPbI_3$ perovskite films, resulting in a reduction of GBs. Since GBs can be a non-radiative recombination centers, optimizing GBs is essential for improving photovoltaic performance. Therefore, the reduced GB density observed in $(FA_{0.8}Cs_{0.2})PbI_3$ is expected to suppress defect-assisted recombination and promote more continuous charge

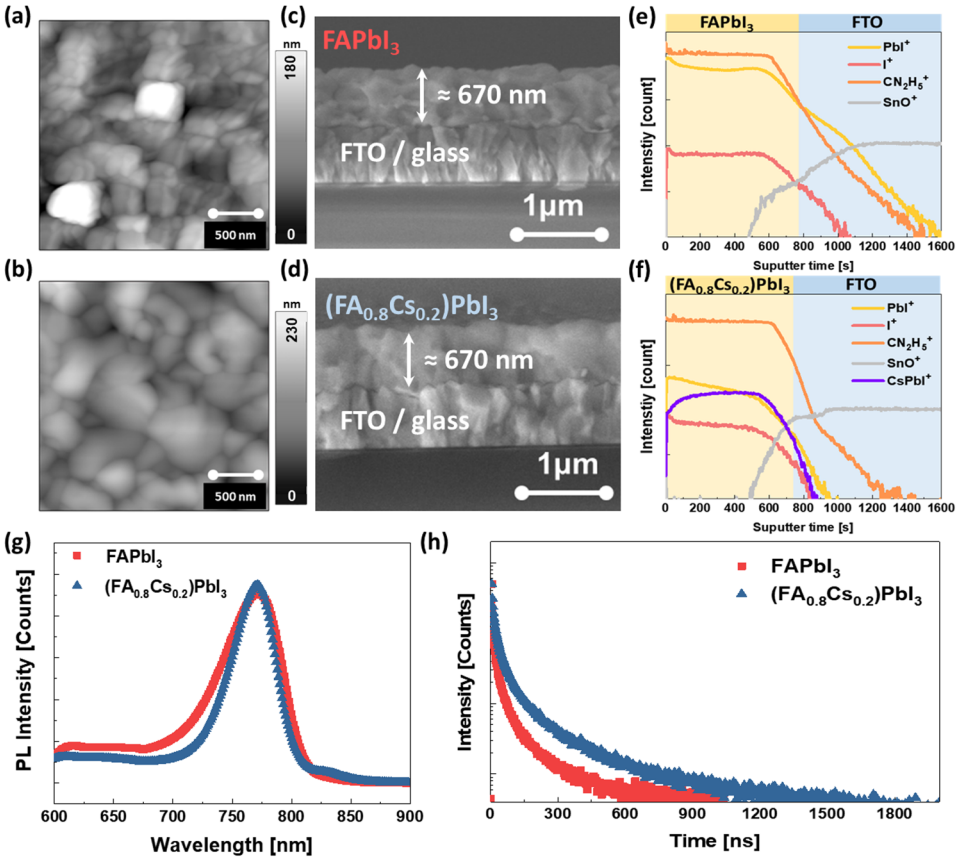


Fig. 4 **a**, **b** Surface topography images obtained from KPFM analyses. **c**, **d** Cross-sectional SEM images of the FTO glass and perovskite layer **e**, **f** Corresponding secondary on mass spectrometry depth profiles of $FAPbI_3$ and $(FA_{0.8}Cs_{0.2})PbI_3$, respectively **g** PL spectrum obtained from the front side of the perovskite film. **h** TRPL spectrum of $FAPbI_3$ and $(FA_{0.8}Cs_{0.2})PbI_3$ perovskite film

transport pathways across the perovskite layer, ultimately increasing J_{SC} and PCE [33–35].

The absorber layer thickness plays a crucial role in determining J_{SC} by governing light absorption and charge carrier collection efficiency [36]. To enable a direct comparison between $FAPbI_3$ and $(FA_{0.8}Cs_{0.2})PbI_3$, the perovskite layer thickness was maintained at 670 nm, as depicted in Fig. 4(c, d). To investigate the nanoscale compositional distribution of constituent ions, particularly the incorporated Cs^+ within the bulk perovskite layer, SIMS analysis was conducted [37]. The signal intensities of PbI^+, I^+, $CN_2H_5^+$ (representing FA^+), SnO^+, and $CsPbI^+$ were measured to evaluate the component distribution once the sequentially deposited PbI_2, FAI, and CsI precursors were annealed. SnO^+ ion analysis confirmed the presence of the FTO substrate. Notably, both $CN_2H_5^+$and $CsPbI^+$ signals maintain a stable and uniform distribution throughout the entire thickness of the perovskite layer. This SIMS profile indicates that the sequentially deposited CsI effectively diffused into the underlying $FAPbI_3$ lattice, achieving a homogeneous $(FA_{0.8}Cs_{0.2})PbI_3$ composition. A comparison between FA^+ ($CN_2H_5^+$) and Cs^+ ($CsPbI^+$) in the $(FA_{0.8}Cs_{0.2})PbI_3$ thin film revealed that FA^+ exhibited a stronger signal intensity, which is qualitatively consistent with the intended nominal composition. (Fig. 4(e, f)).

The PL spectra presented in Fig. 4(g) show a pronounced increase in PL intensity and a narrower full width at half maximum (FWHM), decreasing from 57.42 nm to 45.46 nm, for the $(FA_{0.8}Cs_{0.2})PbI_3$ thin film compared to $FAPbI_3$. The enhanced PL intensity and spectral narrowing indicate suppressed non-radiative recombination channels, which are typically associated with reduced trap density and improved electronic uniformity at the nanoscale [38]. Time-resolved photoluminescence (TRPL) measurements were conducted to further investigate the carrier recombination dynamics. Notably, TRPL spectra were collected from the back side of the device (through the FTO substrate), enabling preferential probing of bulk and buried-interface recombination processes rather than surface-dominated effects. This measurement geometry provides complementary insight to front-side steady-state PL, which is more sensitive to near-surface recombination. The TRPL curves of both samples were fitted by double-exponential decay with fast(τ_1) and slow(τ_2) life-time components.

Through these components, the average carrier lifetime of perovskite thin films was calculated. Increased τ_1 of $(FA_{0.8}Cs_{0.2})PbI_3$ indicates that non-radiative recombination at the surface is suppressed and increased τ_2 of $(FA_{0.8}Cs_{0.2})PbI_3$ suggest that charge carriers in the bulk of perovskite layer survive for a longer period [39]. In Fig. 4(h) and Table 3, $FAPbI_3$ showed both shorter τ_1 (10.3 ns) and τ_2 (73.3 ns) decay components compared to $(FA_{0.8}Cs_{0.2})PbI_3$ (10.3 ns, 73.3 ns), which shows prolonged decay components, indicating suppressed trap-assisted recombination and enhanced bulk carrier lifetime. Consequently, the calculated average carrier lifetime of $(FA_{0.8}Cs_{0.2})PbI_3$ for 39.5 ns is also longer than pure $FAPbI_3$ (23.1 ns). In addition to the prolonged lifetimes, the amplitude ratio (A_2/A_1) extracted from the bi-exponential fitting provides critical insight into the dominant recombination pathways. The increased A_2/A_1 ratio observed in $(FA_{0.8}Cs_{0.2})PbI_3$ indicates that a larger fraction of photogenerated carriers participate in long-lived radiative recombination processes rather than fast trap-assisted decay. This redistribution of carriers toward slow decay component reflects a reduction in defect-mediated recombination centers and an improved nanoscale recombination environment. The consistency between front-side PL enhancement and back-side TRPL lifetime prolongation suggests that Cs incorporation improves both surface-near and bulk recombination dynamics, despite the different probing depths of the two techniques. These results demonstrate that the mixed-cation perovskite exhibits intrinsically improved carrier recombination characteristics across the entire absorber thickness. Overall, the prolonged carrier lifetime and increased A_2/A_1 ratio in $(FA_{0.8}Cs_{0.2})PbI_3$ confirm a reduced defect density and suppressed non-radiative recombination, which directly contribute to enhanced charge carrier collection efficiency and the improved PCE.

KFPM was used to characterize their photovoltaic properties in a non-contact mode using a conducting cantilever tip [40]. The contact potential difference (V_{CPD}) is defined by the following equation [41]:

$$V_{CPD} = \frac{\Delta \Phi}{e} = \frac{\Phi_{tip} - \Phi_{sample}}{e}, \quad (3)$$

where Φ_{tip} is the work function of the cantilever tip, and Φ_{sample} is the work function of the sample.

To further investigate band bending and interface trap states, KPFM measurements were performed under dark and illuminated conditions [42, 43]. The SPV is defined as [44]

$$SPV = V_{CPD_illuminated} - V_{CPD_dark} \quad (4)$$

As illustrated in Fig. 4(b), the films exhibited negative SPV values ((Eq. (4)), which signifies that illumination leads to a decrease in V_{CPD} and a corresponding increase in the surface work function (Φ_{sample}). When electron traps dominate, photogenerated electrons accumulate near the surface. This increased negative charge partially screens the positive space-charge region, mitigates the upward band bending in the n-type semiconductor, and consequently results in a reduced work function under illumination. In contrast, in hole-trap-dominant perovskite thin films, photogenerated electrons are repelled toward the bulk, while the trapped holes accumulate at the interface, reinforcing the positive surface charge [45]. This process induces a more pronounced upward band bending, effectively driving the E_F further away from the vacuum level at the surface. Consequently, the work function increases under illumination (Figure S2). This illumination-induced rise in work function reflects a strengthened near-surface electric field, which promotes more effective charge separation and significantly suppresses interfacial recombination. The degree of band bending can be quantitatively assessed through the shifts in the work-function line profiles extracted from the KPFM measurements. Figure 5(a, b) presents the statistical distribution of V_{CPD} under dark condition and illuminated condition. When SPV is converted to work function shift, the $FAPbI_3$ film showed a relatively small shift amplitude of approximately 0.024 eV, whereas $(FA_{0.8}Cs_{0.2})PbI_3$ exhibited a much larger shift of 0.053 eV (Fig. 5(c)). By calibrating the AFM tip work function using a reference HOPG sample, the measured V_{CPD} was converted into absolute work function values, yielding tip work functions of 4.57 eV for $FAPbI_3$ and 4.40 eV for $(FA_{0.8}Cs_{0.2})PbI_3$. $(FA_{0.8}Cs_{0.2})PbI_3$ displays significantly larger grains and a reduced density of GBs, suggesting a lower concentration of electron traps. With fewer electron traps, trap-assisted recombination is suppressed and the hole accumulation at the surface becomes the dominant factor governing the SPV response. When the occupation of surface hole traps is

Table 3 Parameters of the double-exponential fitting for TRPL decay curves for $FAPbI_3$ and $(FA_{0.8}Cs_{0.2})PbI_3$ perovskite films. The decay curves were fitted using the equation $I(t)=A_1 \exp(-t/\tau_1) + A_2 \exp(-t/\tau_2)$, where τ_1 and τ_2 are the fast and slow decay lifetimes and amplitude ratios (A_2/A_1), respectively. The average carrier lifetime (τ_{avg}) was calculated from the components

	A_1	τ_1 (ns)	A_2	τ_2 (ns)	τ_{avg} (ns)	A_2/A_1
$FAPbI_3$	51237.7	6.1	1653.8	69.4	23.1	0.0323
$(FA_{0.8}Cs_{0.2})PbI_3$	38674.0	10.3	4696.3	73.3	39.5	0.1285

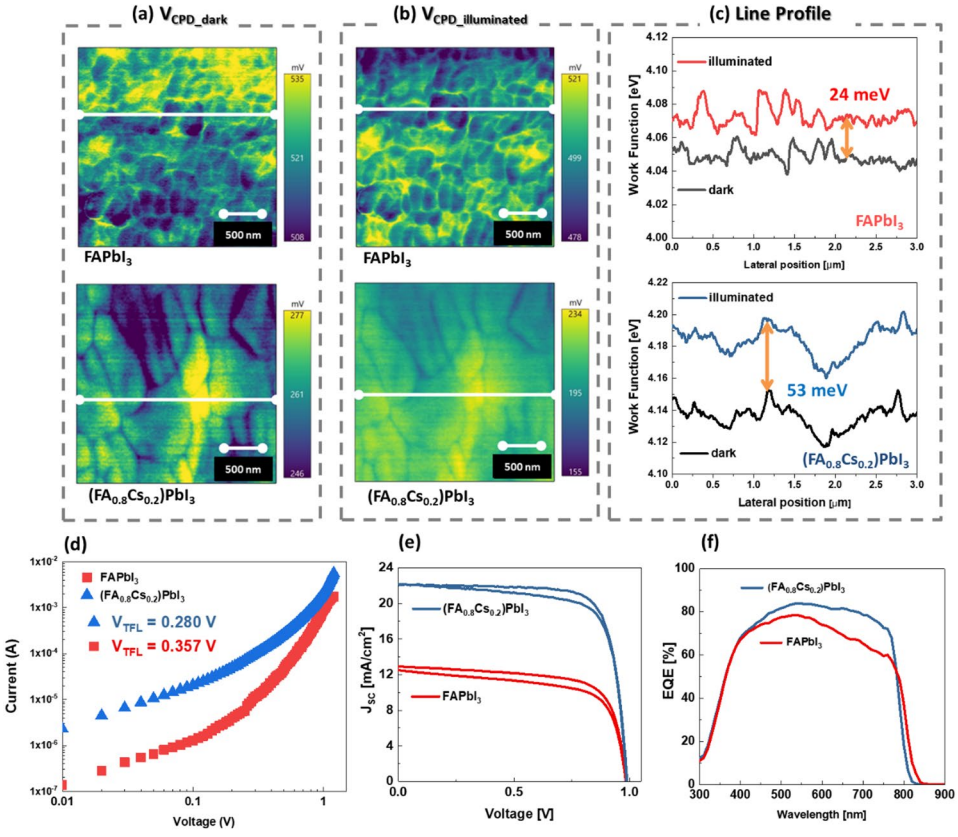


Fig. 5 **a**, **b** Surface potential map images of perovskite thin films obtained from KPFM analyses. SPV of perovskite thin films recorded along the marked line **c** Corresponding line profiles showing the work function shift between dark and illuminated conditions for each film. **d** Dark *J-V* characteristics of the electron-only devices plotted on a log-log scale. The kink point in the curves represents the trap-filled limit voltage (V_{TFL}), from which the N_t is calculated. **e** *J–V* hysteresis curves of best-performing $FAPbI_3$ and $(FA_{0.8}Cs_{0.2})PbI_3$ comparing forward and reverse sweeps. **f** EQE spectrum corresponding to the best-performing PSCs

strengthened, positive charges accumulate in the near the surface, enhancing the upward band bending in n-type thin films. Consequently, the work function increase is more substantial and spatially uniform, leading to the larger SPV. As a result, the larger work function shift in $(FA_{0.8}Cs_{0.2})PbI_3$ corresponds to a deeper Fermi-level shift toward the E_V, implying improved band alignment with the hole transport layer and more efficient interfacial charge extraction. These results confirm that partial substitution of FA^+ with Cs^+ enhances suppresses electron-trap formation.

$$N_t = \frac{2\epsilon_0\epsilon_r V_{TFL}}{qL^2} \quad (5)$$

To quantify the trap density (N_t), the electron-only devices with an n-i-n structure (Figure S3) were fabricated and their dark J-V characteristics were analyzed using the space-charge-limited current method. V_{TFL} is obtained by fitting the log scale dark I-V curve in Fig. 5(d). The kink point that indicates the V_{TFL} are obtained at 0.357 V for $FAPbI_3$ and 0.280 V for $(FA_{0.8}Cs_{0.2})PbI_3$. The trap density (N_t) was calculated via Eq. (5). L (670 nm) is the thickness of perovskite layer, ε_0 is the vacuum permittivity ($8.854\times10^{-12}\ F/m$), and q is the elemental charge (1.602×10^{-19} C). ε_r is the relative dielectric constant of the perovskite thin film, ε_r of $FAPbI_3$ is 46.9 [46]. For the electron-only devices, the trap density of $FAPbI_3$ was 4.13×10^{15} cm^{-3} (V_{TFL} = 0.357 V) and N_t of $(FA_{0.8}Cs_{0.2})PbI_3$ was 3.24×10^{15} cm^{-3} (V_{TFL} = 0.280 V), respectively (Table 4). This quantitative result demonstrates that Cs^+ incorporation effectively passivates defects within the perovskite layer. This reduction in trap density is a critical

Table 4 The trap-filled limit voltage a calculated trap density and for $FAPbI_3$ and $(FA_{0.8}Cs_{0.2})PbI_3$ perovskite thin films. The trap density was calculated using the equation $N_t = \frac{2\epsilon_0\epsilon_r V_{TFL}}{qL^2}$, where q is the elementary charge, L is the thickness of the perovskite layer, ϵ_r is the relative dielectric constant, and ϵ_0 is the vacuum permittivity

	V_{TFL}	N_t
$FAPbI_3$	0.357 V	4.13×10^{15} cm^{-3}
$(FA_{0.8}Cs_{0.2})PbI_3$	0.280 V	3.24×10^{15} cm^{-3}

factor for enhancing device performance. A lower concentration of trap states suppresses non-radiative recombination pathways, allowing photogenerated charge carriers to survive longer and travel further. This leads to an increased carrier lifetime and improved charge collection efficiency, which ultimately contributes to a higher J_{SC}. This finding is in agreement with the TRPL and PL measurements, providing a consistent explanation for the improved device performance.

The *J*–*V* curves of the best two samples were recorded during forward and reverse sweeps (Fig. 5(e)). A noticeable hysteresis effect was observed in the $FAPbI_3$ device, which is often attributed to mobile ion migration and charge trapping at defects or interfaces. In contrast, the $(FA_{0.8}Cs_{0.2})PbI_3$ device exhibited a significantly suppressed hysteresis, indicating stabilized interfacial charge dynamics and reduced defect-assisted ionic motion, consistent with the improved recombination characteristics revealed by TRPL analysis. Additionally, the EQE spectrum was recorded over the 300–900 nm range, covering the primary region of solar energy absorption (Fig. 5(f)). EQE measurements were conducted to evaluate J_{SC} performance [47]. The integrated J_{SC} calculated from the EQE spectrum was 20.69 mA/cm^2 for the $(FA_{0.8}Cs_{0.2})PbI_3$ device, which is notably higher than the 19.02 mA/cm^2 obtained for the $FAPbI_3$ device. This enhancement confirms more efficient charge collection enabled by improved nanoscale electronic properties.

4 Conclusion

In summary, we have fabricated high-efficiency mixed-cation $(FA_{0.8}Cs_{0.2})PbI_3$ PSCs using a sequential TE method. Using sequential TE, we can control precisely over the thickness, deposition rate and partial pressure. Beyond fabrication reproducibility, this work identifies the deposition sequence itself as a critical nanoscale control parameter that governs cation distribution, phase evolution, and electronic uniformity in vacuum-processed perovskite thin films. Depositing the organic material first (FAI) and then the inorganic material (CsI) deposited as the final layer provides a deterministic pathway for solid-state Cs^+ diffusion into the entire perovskite bulk, which was confirmed by depth-profiled SIMS analysis. This controlled diffusion enables a spatially uniform A-site cation distribution. The addition of Cs^+ to the $FAPbI_3$ lattice shifted the Goldschmidt tolerance factor closer to 1, stabilizing the perovskite lattice and promoting the formation of a highly crystalline α-phase, as confirmed by XRD analysis. The structural optimization induced by controlled Cs^+ incorporation leads to larger and more uniform grains with a reduced density of GBs, thereby suppressing defect-assisted non-radiative recombination pathways. These improvements in the defect and crystalline quality are consistently supported by PL, TRPL, and KPFM-SPV analyses, which reveal prolonged carrier lifetimes, enhanced radiative recombination probability, and a stabilized local electrostatic potential under illumination. Consequently, the $(FA_{0.8}Cs_{0.2})PbI_3$ based device shows higher photocurrent generation and a clear enhancement in photovoltaic performance. In details, the results show a significant improvement in J_{SC} (from 11.754 mA/cm^2 to 20.705 mA/cm^2) and FF (from 63.9% to 74.1%) with optimal Cs content, consequently, the dramatic increase in PCE from 8.89% to 16.88%. Overall, this study demonstrates that the deposition sequence in sequential TE critically governs cation diffusion and phase stability in perovskite thin films. The optimized Cs content enables uniform cation intermixing during annealing and stable α-phase formation, while Cs^+ incorporation further enhances lattice stability and charge transport. These results highlight that precise control of deposition order and cation incorporation is key to achieving phase-stable and high-performance perovskite solar cells.

Abbreviation

$FAPbI_3$	Formamidinium lead iodide
$CsPbI_3$	Cesium lead iodide
PSCs	Perovskite solar cells
TE	Thermal evaporation
KPFM	Kelvin probe force microscopy
EQE	External quantum efficiency
V_{OC}	Open-Circuit Voltage
J_{SC}	Short-Circuit Current Density
FF	Fill Factor
PCE	Power conversion efficiency
E_g	Band gap
V_{CPD}	Contact potential difference
GB	Grain boundary
SPV	Surface photovoltage
FWHM	Full width at half maximum
V_{TFL}	Trap-filled limit voltage

Supplementary Information

The online version contains supplementary material available at https://doi.org/10.1186/s40580-026-00541-5.

Supplementary Material 1

Acknowledgements
Not applicable.

Author contributions
YG and WJ wrote the manuscript, analyzed the data, interpreted the results, and designed the experiments. YG, HKP and YSK also set up and designed the experimental apparatus. YG carried out most of the experiments. GL and JK contributed significantly to the KPFM and SPV measurements and their subsequent analysis. WJ supervised the entire project. All authors read and approved the final manuscript.

Funding
This work was supported by the National Research Foundation of Korea (NRF) grant funded by the Korea government (MSIT and MOE) (No. RS-2025-16063688). This research was supported by the NRF funded by the Ministry of Science and ICT (RS-2024-00355905) and the NRF under grants NRF

(RS-2018-NR031064). Additionally, the work was supported by the Ewha Womans University Research Grant of 2025.

Data availability
Not applicable.

Declarations

Competing interests
The authors declare they have no competing interests.

Author details
[1]Department of Physics, Ewha Womans University, Seoul 03760, Republic of Korea
[2]Institute of Multiscale Matter and System (IMMS), Ewha Womans University, Seoul 03760, Republic of Korea
[3]New and Renewable Energy Research Center, Ewha Womans University, Seoul 03760, Korea
[4]Advanced Institute of Convergence Technology, Suwon 16229, Korea

Received: 27 January 2026 / Accepted: 14 February 2026
Published online: 21 February 2026

References

1. N.S. Kumar, K.C.B. Naidu, A review on perovskite solar cells (PSCs), materials and applications. J. Materiomics. **7**, 940–956 (2021). https://doi.org/10.1016/j.jmat.2021.04.002
2. S. Bello, A. Urwick, F. Bastianini, A.J. Nedoma, A. Dunbar, An introduction to perovskites for solar cells and their characterisation. Energy Rep. **8**, 89–106 (2022). https://doi.org/10.1016/j.egyr.2022.08.205
3. I. Diomandé, A. Bouich, A.A. Hyacinthe, B.M. Soucasse, A. Boko, Comparative Performance Analysis of MAPbI3 and FAPbI3 Perovskites: study of Optoelectronic Properties and Stability. Model. Numer. Simul. Mater. Sci. **13**, 51–67 (2023). https://doi.org/10.4236/mnsms.2023.134004
4. Z. Liu, P. Liu, M. Li, T. He, T. Liu, L. Yu et al., Efficient and stable FA-rich perovskite photovoltaics: from material properties to device optimization. Adv. Energy Mater. **12**, 2200111 (2022). https://doi.org/10.1002/aenm.202200111
5. H. Lee, S.B. Kang, S. Lee, K. Zhu, D.H. Kim, Progress and outlook of Sn–Pb mixed perovskite solar cells. Nano Convergence. **10**, 27 (2023). https://doi.org/10.1186/s40580-023-00371-9
6. Y. Huang, K. Yan, X. Wang, B. Li, B. Niu, M. Yan et al., High-efficiency inverted perovskite solar cells via in situ passivation directed crystallization. Adv. Mater. **36**, 2408101 (2024). https://doi.org/10.1002/adma.202408101
7. J. Kim, W. Jo, Engineering of buried interfaces in perovskites: advancing sustainable photovoltaics. Nano Convergence. **11**, 1–26 (2024). https://doi.org/10.1186/s40580-024-00464-z
8. H. Li, J. Zhou, L. Tan, M. Li, C. Jiang, S. Wang et al., Sequential vacuum-evaporated perovskite solar cells with more than 24% efficiency. Sci. Adv. **8**, eabo7422 (2022). https://doi.org/10.1126/sciadv.abo7422
9. H. Li, M. Liu, M. Li, H. Park, N. Mathews, Y. Qi et al., Applications of vacuum vapor deposition for perovskite solar cells: a progress review. *IEnergy* 1, 434 – 52 (2022). https://doi.org/10.23919/IEN.2022.0053
10. P. Wu, J. He, F. Zhang, Vacuum thermal evaporation saved MA-free perovskite. Joule. **6**, 1394–1396 (2022). https://doi.org/10.1016/j.joule.2022.06.010
11. F.U. Kosasih, E. Erdenebileg, N. Mathews, S.G. Mhaisalkar, A. Bruno, Thermal evaporation and hybrid deposition of perovskite solar cells and mini-modules. Joule. **6**, 2692–2734 (2022). https://doi.org/10.1016/j.joule.2022.11.004
12. N. Kumari, S.R. Patel, J.V. Gohel, Superior efficiency achievement for FAPbI3-perovskite thin film solar cell by optimization with response surface methodology technique and partial replacement of Pb by Sn. *Optik* 176, 262 – 77 (2019). https://doi.org/10.1016/j.ijleo.2018.09.066
13. M. Noman, M. Shahzaib, S.T. Jan, S.N. Shah, A.D. Khan, 26.48% efficient and stable FAPbI 3 perovskite solar cells employing SrCu 2 O 2 as hole transport layer. RSC Adv. **13**, 1892–1905 (2023). https://doi.org/10.1039/d2ra06535e
14. S. Li, Y. Jiang, J. Xu, D. Wang, Z. Ding, T. Zhu et al., High-efficiency and thermally stable FACsPbI3 perovskite photovoltaics. Nature. **635**, 82–88 (2024). https://doi.org/10.1038/s41586-024-08103-7
15. S. Hu, A.R. Tapa, X. Zhou, S. Pang, M. Lira-Cantu, H. Xie, Formation and stabilization of metastable halide perovskite phases for photovoltaics. Cell. Rep. Phys. Sci. **5** (2024). https://doi.org/10.1016/j.xcrp.2024.101825
16. L. Gil-Escrig, C. Dreessen, F. Palazon, Z. Hawash, E. Moons, S. Albrecht et al., Efficient wide-bandgap mixed-cation and mixed-halide perovskite solar cells by vacuum deposition. *ACS energy letters* 6, 827 – 36 (2021). https://doi.org/10.1021/acsenergylett.0c02445
17. R. Kottokkaran, H.A. Gaonkar, B. Bagheri, V.L. Dalal, Efficient pin inorganic CsPbI3 perovskite solar cell deposited using layer-by-layer vacuum deposition. J. Vacuum Sci. Technol. A **36** (2018). https://doi.org/10.1116/1.5029253
18. F. Ma, J. Li, W. Li, N. Lin, L. Wang, J. Qiao, Stable α/δ phase junction of formamidinium lead iodide perovskites for enhanced near-infrared emission. Chem. Sci. **8**, 800–805 (2017). https://doi.org/10.1039/c6sc03542f
19. Y. Zhang, S.G. Kim, D.K. Lee, N.G. Park, CH3NH3PbI3 and HC (NH2) 2PbI3 Powders Synthesized from Low-Grade PbI2: single Precursor for High-Efficiency Perovskite Solar Cells. *ChemSusChem* 11, 1813-23 (2018). https://doi.org/10.1002/cssc.201800610
20. J. Zhao, S.O. Fürer, D.P. McMeekin, Q. Lin, P. Lv, J. Ma et al., Efficient and stable formamidinium–caesium perovskite solar cells and modules from lead acetate-based precursors. Energy Environ. Sci. **16**, 138–147 (2023). https://doi.org/10.1039/D2EE01634F
21. Z. Wu, S. Sang, J. Zheng, Q. Gao, B. Huang, F. Li et al., Crystallization kinetics of hybrid perovskite solar cells. Angew. Chem. Int. Ed. **63**, e202319170 (2024). https://doi.org/10.1002/anie.202319170
22. Q. Chen, N. De Marco, Y.M. Yang, T.-B. Song, C.-C. Chen, H. Zhao et al., Under the spotlight: The organic–inorganic hybrid halide perovskite for optoelectronic applications. Nano Today. **10**, 355–396 (2015). https://doi.org/10.1016/j.nantod.2015.04.009
23. G. Kieslich, S. Sun, A.K. Cheetham, An extended tolerance factor approach for organic–inorganic perovskites. Chem. Sci. **6**, 3430–3433 (2015). https://doi.org/10.1039/c5sc00961h
24. L. Dimesso, A. Quintilla, Y.-M. Kim, U. Lemmer, W. Jaegermann, Investigation of formamidinium and guanidinium lead tri-iodide powders as precursors for solar cells. Mater. Sci. Engineering: B **204**, 27–33 (2016). https://doi.org/10.1016/j.mseb.2015.11.006
25. Q. Yuan, K.B. Lohmann, R.D. Oliver, A.J. Ramadan, S. Yan, J.M. Ball et al., Thermally stable perovskite solar cells by all-vacuum deposition. ACS Appl. Mater. Interfaces. **15**, 772–781 (2022). https://doi.org/10.1021/acsami.2c14658
26. Y. Sun, J. Peng, Y. Chen, Y. Yao, Z. Liang, Triple-cation mixed-halide perovskites: towards efficient, annealing-free and air-stable solar cells enabled by Pb (SCN) 2 additive. Sci. Rep. **7**, 46193 (2017). https://doi.org/10.1038/srep46193
27. W. Wu, Y. Liu, J. Yao, X. Ouyang, Mixed-cation halide perovskite doped with Rb + for highly efficient photodetector. Materials. **16**, 3796 (2023). https://doi.org/10.3390/ma16103796
28. H. Chen, Y. Chen, T. Zhang, X. Liu, X. Wang, Y. Zhao, Advances to high-performance black-phase FAPbI3 perovskite for efficient and stable photovoltaics. Small Struct. **2**, 2000130 (2021). https://doi.org/10.1002/sstr.202000130
29. F. Cordero, F. Craciun, F. Trequattrini, A. Generosi, B. Paci, A.M. Paoletti et al., Stability of cubic FAPbI3 from X-ray diffraction, anelastic, and dielectric measurements. J. Phys. Chem. Lett. **10**, 2463–2469 (2019). https://doi.org/10.1021/acs.jpclett.9b00896
30. D.T. Cuzzupè, F. Ünlü, K. Lê, R. Bernhardt, M. Wilhelm, M. Grosch et al., Thermally-induced drift of A-site cations at solid–solid interface in physically paired lead halide perovskites. Sci. Rep. **12**, 10241 (2022). https://doi.org/10.1038/s41598-022-14452-y
31. S. Chen, L. Pan, T. Ye, N. Lei, Y. Yang, X. Wang, The lattice reconstruction of Cs-introduced FAPbI 1.80 Br 1.20 enables improved stability for perovskite solar cells. RSC Adv. **11**, 3997–4005 (2021). https://doi.org/10.1039/d0ra09294k
32. R. Jono, H. Segawa, Theoretical study of the band-gap differences among lead triiodide perovskite materials: CsPbI3, MAPbI3, and FAPbI3. Chem. Lett. **48**, 877–880 (2019). https://doi.org/10.1246/cl.190256
33. A.F. Castro-Méndez, J. Hidalgo, J.P. Correa-Baena, The role of grain boundaries in perovskite solar cells. Adv. Energy Mater. **9**, 1901489 (2019). https://doi.org/10.1002/aenm.201901489
34. Z. Chu, M. Yang, P. Schulz, D. Wu, X. Ma, E. Seifert et al., Impact of grain boundaries on efficiency and stability of organic-inorganic trihalide perovskites. Nat. Commun. **8**, 2230 (2017). https://doi.org/10.1038/s41467-017-02331-4
35. S. Iftiquar, J. Yi, Impact of grain boundary defect on performance of perovskite solar cell. Mater. Sci. Semiconduct. Process. **79**, 46–52 (2018). https://doi.org/10.1016/j.mssp.2018.01.022
36. A. Mortadi, E. El Hafidi, M. Monkade, R.E. Moznine, Investigating the influence of absorber layer thickness on the performance of perovskite solar cells: a

combined simulation and impedance spectroscopy study. Mater. Sci. Energy Technol. **7**, 158–165 (2024). https://doi.org/10.1016/j.mset.2023.10.001
37. J. Ekar, P. Panjan, S. Drev, J. Kovač, ToF-SIMS depth profiling of metal, metal oxide, and alloy multilayers in atmospheres of H2, C2H2, CO, and O2. J. Am. Soc. Mass. Spectrom. **33**, 31–44 (2021). https://doi.org/10.1021/jasms.1c00218
38. H. Zalrhi, M. Ouafi, M. Regragui, B.M. Soucase, F. Baig, Y.H. Khattak et al., Improving photoluminescence properties and reducing recombination of CsPbBr 3 perovskite through lithium doping. RSC Adv. **14**, 15048–15057 (2024). https://doi.org/10.1039/d4ra01548g
39. H. Kim, J.W. Lee, G.R. Han, Y.J. Kim, S.H. Kim, S.K. Kim et al., Highly efficient hole transport layer-free low bandgap mixed Pb–Sn perovskite solar cells enabled by a binary additive system. Adv. Funct. Mater. **32**, 2110069 (2022). https://doi.org/10.1002/adfm.202110069
40. C. Lu, Z. Hu, Y. Wang, K. Sun, B. Shen, C. Gao et al., Carrier transfer behaviors at perovskite/contact layer heterojunctions in perovskite solar cells. Adv. Mater. Interfaces. **6**, 1801253 (2019). https://doi.org/10.1002/admi.201801253
41. B.P. Nguyen, H.R. Jung, J. Kim, W. Jo, Enhanced carrier transport over grain boundaries in lead-free CH3NH3Sn (I1 – xBrx) 3 (0 ≤ x ≤ 1) perovskite solar cells. Nanotechnology. **30**, 314005 (2019). https://doi.org/10.1088/1361-6528/ab19dd
42. W. Zhang, S. Pathak, N. Sakai, T. Stergiopoulos, P.K. Nayak, N.K. Noel et al., Enhanced optoelectronic quality of perovskite thin films with hypophosphorous acid for planar heterojunction solar cells. Nat. Commun. **6**, 10030 (2015). https://doi.org/10.1038/ncomms10030
43. J. Kim, J.S. Park, G.Y. Kim, W. Jo, Autonomous Control of Ion Migration at α-FAPbI3 Heterointerfaces via Interfacial-Self-Assembled 2D Perovskite. Adv. Energy Mater. **14**, 2402117 (2024). https://doi.org/10.1002/aenm.202402117
44. Z. Zhang, J.T. Jr Yates, Band bending in semiconductors: chemical and physical consequences at surfaces and interfaces. Chem. Rev. **112**, 5520–5551 (2012). https://doi.org/10.1021/cr3000626
45. D. Cavalcoli, B. Fraboni, A. Cavallini, Surface and defect states in semiconductors investigated by surface photovoltage. In: Semiconductors and Semimetals. 91 Elsevier; 2015. pp. 251 – 78. https://doi.org/10.1016/bs.semsem.2014.11.004
46. Q. Han, S.H. Bae, P. Sun, Y.T. Hsieh, Y. Yang, Y.S. Rim et al., Single crystal formamidinium lead iodide (FAPbI3): insight into the structural, optical, and electrical properties. Adv. Mater. **28**, 2253–2258 (2016). https://doi.org/10.1002/adma.201505002
47. H. Zhang, S. Zhang, X. Ji, J. He, H. Guo, S. Wang et al., Formamidinium Lead Iodide-Based Inverted Perovskite Solar Cells with Efficiency over 25% Enabled by An Amphiphilic Molecular Hole-Transporter. Angew. Chem. **136**, e202401260 (2024). https://doi.org/10.1002/anie.202401260

Publisher's note

Springer Nature remains neutral with regard to jurisdictional claims in published maps and institutional affiliations.